The Astrophysical Journal, 873:99 (11pp), 2019 March 1 https://doi.org/10.3847/1538-4357/ab0414

NuSTAR Observations of the Accreting Atolls GX 3+1, 4U 1702-429, 4U 0614+091, and 4U 1746-371

R. M. Ludlam[1], J. M. Miller[1], D. Barret[2,3], E. M. Cackett[4], B. M. Coughenour[4], T. Dauser[5], N. Degenaar[6], J. A. García[5,7], F. A. Harrison[7], and F. Paerels[8]
[1] Department of Astronomy, University of Michigan, 1085 South University Avenue, Ann Arbor, MI 48109-1107, USA
[2] Université de Toulouse; UPS-OMP; IRAP; Toulouse, France
[3] CNRS; Institut de Recherche en Astrophysique et Plantologie; 9 Av. colonel Roche, BP 44346, F-31028 Toulouse cedex 4, France
[4] Department of Physics & Astronomy, Wayne State University, 666 W. Hancock Street, Detroit, MI 48201, USA
[5] Remeis Observatory & ECAP, Universität Erlangen-Nürnberg, Sternwartstr. 7, D-96049, Bamberg, Germany
[6] Anton Pannekoek Institute for Astronomy, University of Amsterdam, Pastbus 94249, 1090 GE Amsterdam, The Netherlands
[7] Cahill Center for Astronomy and Astrophysics, California Institute of Technology, Pasadena, CA 91125, USA
[8] Columbia Astrophysics Laboratory, 550 West 120th Street, New York, NY 10027, USA
Received 2018 July 12; revised 2019 January 30; accepted 2019 January 31; published 2019 March 7

Abstract

Atoll sources are accreting neutron star (NS) low-mass X-ray binaries. We present a spectral analysis of four persistent atoll sources (GX 3+1, 4U 1702−429, 4U 0614+091, and 4U 1746−371) observed for ∼20 ks each with *NuSTAR* to determine the extent of the inner accretion disk. These sources range from an apparent luminosity of 0.006–0.11 of the Eddington limit (assuming the empirical limit of 3.8×10^{38} erg s^{-1}). Broad Fe emission features shaped by Doppler and relativistic effects close to the NS were firmly detected in three of these sources. The position of the disk appears to be close to the innermost stable circular orbit (ISCO) in each case. For GX 3+1, we determine $R_{\rm in} = 1.8^{+0.2}_{-0.6}\ R_{\rm ISCO}$ (90% confidence level) and an inclination of 27°–31°. For 4U 1702−429, we find a $R_{\rm in} = 1.5^{+1.6}_{-0.4}\ R_{\rm ISCO}$ and inclination of 53°–64°. For 4U 0614+091, the disk has a position of $R_{in} = 1.3^{+5.4}_{-0.2}\ R_{\rm ISCO}$ and inclination of 50°–62°. If the disk does not extend to the innermost stable circular orbit, we can place conservative limits on the magnetic field strength in these systems in the event that the disk is truncated at the Alfvén radius. This provides the limit at the poles of $B \leqslant 6.7 \times 10^8$ G, 3.3×10^8 G, and 14.5×10^8 G for GX 3+1, 4U 1702−429, and 4U 0614+091, respectively. For 4U 1746−371, we argue that the most plausible explanation for the lack of reflection features is a combination of source geometry and strong Comptonization. We place these sources among the larger sample of NSs that have been observed with *NuSTAR*.

Key words: accretion, accretion disks – stars: neutron – stars: individual (GX 3+1, 4U 1746-371, 4U 1702-429, 4U 0614+091) – X-rays: binaries

1. Introduction

Accretion onto compact objects in low-mass X-ray binaries (LMXBs) occurs via a disk that formed through Roche-lobe overflow from the envelope of the roughly stellar mass companion star. Persistently accreting neutron star (NS) LMXBs are separated into two categories: "Z" and "atoll." These classifications derive their name from the shape they trace out in color–color and hardness-intensity diagrams (Hasinger & van der Klis 1989). Z sources are very luminous as they likely accrete at near Eddington luminosities (0.5–1.0 $L_{\rm Edd}$: van der Klis 2005), whereas atoll sources are typically less luminous (∼0.001–0.5 $L_{\rm Edd}$). Transient systems that alternate between periods of active accretion and quiescence often exhibit atoll-like or Z-like behavior during outburst. Some sources are even able to transition between the two classes (e.g., XTE J1701−462, Homan et al. 2010) suggesting a trend with average mass accretion rate.

Atoll sources generally have two spectral states analogous to black hole (BH) LMXBs: (1) a hard state characterized by power-law emission with little thermal emission, and (2) a soft state dominated by thermal emission. Additionally, they show intermediate behavior as the sources transition between these states (see Wijnands et al. 2017 for a recent discussion on the detailed morphology).

Lin et al. (2007) analyzed the spectrum of two atoll type transients (Aquila X-1 and 4U 1608−52) to devise a "hybrid" model for the hard and soft spectral states. The hard state can be described by a single-temperature blackbody to account for boundary layer emission (where material from the disk reaches the surface of the NS) and a power-law component to account for Comptonization. The soft state can be described by a double thermal model comprised of a multitemperature blackbody for disk emission and a single-temperature blackbody with the addition of a power-law component. This provided a coherent picture of the spectral evolution (e.g., the thermal components follow $L_{\rm X} \propto T^4$) and timing behavior of these sources that is analogous to BHs, which has been utilized for a number of other NS LMXBs (e.g., Cackett et al. 2008, 2009, 2010; Lin et al. 2010; Miller et al. 2013; Chiang et al. 2016a).

The hard X-ray photons that originate from the boundary layer or coronal region can illuminate the disk and be reprocessed by the material therein before being re-emitted. This reprocessed emission is known as the "reflection" spectrum. Doppler and relativistic effects are imprinted on features in the reflection spectrum, such as Fe K_α, yielding information about accretion flow (Fabian et al. 1989). The strength of these effects increases with proximity to the compact object, thus allowing the position of the inner accretion disk to be determined from the shape of the Fe line profile. The accretion disk around an NS has to truncate at or prior to the surface, hence reflection studies in NS LMXBs can provide upper limits on the radial extent of these objects

(Cackett et al. 2008; Miller et al. 2013; Ludlam et al. 2017a) or indicate the presence of a boundary layer or strong magnetic field (Cackett et al. 2009; Papitto et al. 2009; King et al. 2016; Ludlam et al. 2017b, 2017c; van den Eijnden et al. 2017).

The location of the inner edge of the accretion disk around compact objects is thought to be dependent on the mass accretion rate, $\dot{m}$, of the system (González Martínez-País et al. 2014 for a review). Indeed, the overall spectral evolution of atolls does change with $\dot{m}$ (Gladstone et al. 2007), but there does not appear to be a clear one-to-one correlation with the inner disk position (Cackett et al. 2010; Chiang et al. 2016a; Ludlam et al. 2017a). When looking at a sample of NS LMXBs from which the inner disk radius could be determined via reflection, some atoll sources were consistent with the innermost stable circular orbit (ISCO) at as low as 1% $L_{\rm Edd}$, whereas others were truncated at higher accretion rates near 10% $L_{\rm Edd}$ (Ludlam et al. 2017a). This suggests a more complex behavior for the position on the inner accretion disk that relies on more than just $\dot{m}$ (e.g., the importance of the magnetosphere or boundary layer).

We present a sample of four persistently accreting atoll sources that were approved an initial ∼20 ks observation each with *NuSTAR* (Harrison et al. 2013) during GO Cycle 3: GX 3+1, 4U 1702−429, 4U 0614+091, and 4U 1746−371. We search for the presence of reflection features and place constraints on the position of the inner disk. *NuSTAR* has been an exceptional tool for reflection studies due to its large energy bandpass from 3 to 79 keV, as well as its high effective collecting area that is free from instrumental effects such as pile-up. Our sample spans the range of 0.006–0.11 $L_{\rm Edd}$, assuming the empirical Eddington limit of 3.8×10^{38} erg s^{-1}(Kuulkers et al. 2003). The paper is structured in the following format: the subsequent subsections provide background on each source (Sections 1.1–1.4), Section 2 presents the observations and data reduction, Section 3 discusses the spectral analysis and results, Section 4 provides a discussion of the results, Section 5 summarizes the discussion.

1.1. GX 3+1

GX 3+1 is known to exhibit both Type-I X-ray bursts (Makishima et al. 1983; Kuulkers & van der Klis 2000; Chenevez et al. 2006) and longer duration superbursts from carbon burning (Kuulkers 2002). Imposing the assumption that the Type-I X-ray bursts are Eddington limited provides a maximum distance to the source of 6.5 kpc (Galloway et al. 2008). A broad Fe line was first detected in this source with *Beppo*SAX (Oosterbroek et al. 2001). *XMM-Newton* observations of the source confirmed the presence of a relativistically shaped Fe line and revealed potential lower-energy features due to Ar XVIII and Ca XIX (Piraino et al. 2012). The Fe line profile suggested that the inner disk was located at a distance of $\sim 25\,R_g$ (where $R_g = GM/c^2$) with an inclination of 35°–44° when fit with a simple DISKLINE model (Fabian et al. 1989). Pintore et al. (2015) analyzed *XMM-Newton* and *INTEGRAL* observations from 2010 which suggested that the disk was closer to the NS at $\sim 10\,R_g$ with an inclination of ∼35° when accounting for the entire reflection spectrum.

1.2. 4U 1702−429

4U 1702−429 is a burster (Swank et al. 1976) located at a maximum distance of 5.65 kpc (Galloway et al. 2008), assuming that the Type-I X-ray bursts are Eddington limited. Burst oscillations were detected at a frequency of 330 Hz with the *Rossi X-ray Timing Explorer* (*RXTE*; Markwardt et al. 1999), which is indicative of the spin frequency of the NS. This spin frequency corresponds to a dimensionless spin parameter ($a = cJ/GM^2$) of 0.155 (Braje et al. 2000), assuming an NS mass of 1.4 $M_\odot$, a 10 km radius, and softish equation of state of the "FPS" model (Cook et al. 1994). Iaria et al. (2016) provided the first investigation of the broadband spectrum using observations from both *XMM-Newton* and *INTEGRAL*. This revealed a broad Fe line component that originated from a significantly truncated disk with an inner disk radius of $31^{+25}_{-12}\ R_g$ and implied an inclination of $44^{+33\circ}_{-6}$.

1.3. 4U 0614+091

4U 0614+091 is an ultracompact X-ray binary with an orbital period of ∼50 minutes (Shahbaz et al. 2008) located at a distance of 3.2 kpc (Kuulkers et al. 2010). Type-I X-ray bursts have been detected in this system (Swank et al. 1978; Brandt et al. 1992) confirming that the compact object is an NS. A spin frequency of 415 Hz (Strohmayer et al. 2008) was determined from burst oscillations, which translates to $a = 0.2$ using the formalism from Braje et al. (2000). The companion star is either a CO or ONe white dwarf due to carbon and oxygen emission lines present in the optical spectrum (Nelemans et al. 2004). Madej et al. (2010) detected relativistically broadened O VIII Ly$_\alpha$ emission in the *XMM-Newton* Reflection Grating Spectrometer detectors. When modeling the O VIII Ly$_\alpha$ emission with a relativistic line profile, this emission appeared to originate from the innermost region ($\sim 6\,R_g$) of a highly inclined disk ($i \approx 54°$). A follow-up study using the *XMM-Newton*/EPIC-pn data additionally revealed the presence of an Fe line feature (Madej et al. 2014). Spectral modeling of both features via a specially tailored reflection spectrum model for an overabundance of C and O, XILLVER$_{\rm CO}$, supported the previous results of a disk close to the ISCO with a moderate inclination.

1.4. 4U 1746−371

4U 1746−371 is associated with the globular cluster NGC 6441. Variable stars in the cluster establish the distance to NGC 6441 to between 10.4 and 11.9 kpc (Pritzl et al. 2001). The source is known to experience Type-I X-ray bursts (Sztajno et al. 1987) and is a dipping source (Parmar et al. 1989), which indicates that the system is highly inclined. The periodicity of the dipping observed with *Ginga* suggested an orbital period of ∼5.7 hr (Sansom et al. 1993), but follow-up studies with *RXTE* found a smaller period of 5.16 ± 0.01 hr (Bałucińska-Church et al. 2004). *Hubble Space Telescope* imaging of the globular cluster identified five possible optical counterparts, but the field was too dense to isolate a single counterpart as the companion to 4U 1746−371 (Deutsch et al. 1998). Asai et al. (2000) found evidence of a potential narrow Fe line in *ASCA* data, whereas a later investigation by Díaz Trigo et al. (2006) with *XMM-Newton* suggested a broad Fe emission component (modeled with a Gaussian at 6.4 keV that provided a 3.5σ improvement) with a potential narrow Fe XXVI absorption line.

2. Observations and Data Reduction

Table 1 provides the ObsIDs, date, exposure time, and net count rate of each *NuSTAR* observation. We followed the

Table 1
NuSTAR Observation Information

Source	Mission	Obs ID	Date (yyyy-mm-dd)	Exp (ks)	Net Rate (cts s^{-1})
GX 3+1	*NuSTAR*	30363001002	2017 Oct 17	13.7	147.9
4U 1702−429	*NuSTAR*	30363005002	2017 Aug 29	21.7	97.1
4U 0614+091	*NuSTAR*	30363002002	2017 Dec 1	15.1	28.3
4U 1746−371	*NuSTAR*	30363004002	2018 Feb 10	19.8	10.7

standard data reduction procedures using NUSTARDAS v1.8.0 with CALDB 20180126 for each observation. GX 3+1 and 4U 0614+091 required additional parameters to be called when utilizing the NUPIPELINE tool. GX 3+1 is considered a formally bright source for *NuSTAR* (>100 counts s^{-1}), so we applied STATUSEXPR="STATUS==b0000xxx00xxxx000" to correct for high count rates. The observation of 4U 0614+091 occurred during high intervals of background near the South Atlantic Anomaly (SAA); therefore, we imposed SAACALC=3, SAAMODE=strict, and TENTACLE=yes to reduce these periods. Using the NUPRODUCTS tool we created light curves and spectra for each observation using a circular extraction region with a radius of 100″ centered around the source to produce a source spectrum for both the Focal Plane Modules (FPMA and FPMB). We use another 100″ radial region away from the source for the purpose of background subtraction. No Type-I X-ray bursts were present in the light curves. Although it is not generally recommended to combine data from the FPMA/B because the introduced systematics may be larger than the statistical errors in high signal-to-noise observations, most of the sources in our sample have a low signal-to-noise. Therefore, we combine the FPMA/B using ADDASCASPEC to improve the signal-to-noise and provide a uniform analysis among sources in this sample. The data were binned by a factor of 3 using GRPPHA (Choudhury et al. 2017).

3. Spectral Analysis and Results

We use XSPEC version 12.9.1 m (Arnaud 1996) to perform our spectral analysis. Errors are generated from Monte Carlo Markov Chains of length 500,000 in order to simultaneously probe the entire χ^2 parameter space and quoted at the 90% confidence level. We use TBABS (Wilms et al. 2000) to account for absorption along the line of sight to each source with the abundance set to WILM (Wilms et al. 2000) and VERN cross-sections (Verner et al. 1996). The upper limit on the energy range in which each source is modeled is background limited.

Since the *NuSTAR* low-energy bandpass cuts off at 3 keV, we are unable to constrain the absorption column along the line of sight. We utilize archival *XMM-Newton*/RGS data to fit absorption edges with TBNEW[9] to determine $N_{\rm H}$ for each source. Note that these observations are not simultaneous with our *NuSTAR* observations. The RGS data were fit in the 0.45–2.1 keV energy range. We find $N_{\rm H} = 2.42 \pm 0.02 \times 10^{22}\,{\rm cm}^{-2}$ for GX 3+1, $N_{\rm H} = 2.32 \pm 0.06 \times 10^{22}\,{\rm cm}^{-2}$ for 4U 1702−429, $N_{\rm H} = 3.46 \pm 0.01 \times 10^{21}\,{\rm cm}^{-2}$ for 4U 0614+091, and $N_{\rm H} = 3.76 \pm 0.01 \times 10^{21}\,{\rm cm}^{-2}$ for 4U 1746−371. We compare these values to those reported in previous studies on these sources and find good agreement (e.g., GX 3+1: Pintore et al. 2015, 4U 1702−429: Mazzola et al. 2019, 4U 0614+091: Madej et al. 2010, 2014, 4U 1746−371: Díaz Trigo et al. 2006). We therefore fix $N_{\rm H}$ in the following *NuSTAR* fits because column density is dominated by the interstellar medium and does not vary with spectral state (Miller et al. 2009). This is certainly true for low inclination sources, but there can be deviations for high inclination sources due to obscuration within the system itself during dips or eclipses. However, note that the higher inclination sources in this sample do not show dips during our observations.

The continuum is modeled based upon the prescription in Lin et al. (2007) for atoll sources. This is largely motivated by the existence of self-consistent reflection models based upon these components. We check, when appropriate, that our choice of continuum does not bias our results. Only GX 3+1 showed a very soft spectrum consistent with the soft state. The spectrum was modeled with a multitemperature blackbody (DISKBB; Mitsuda et al. 1984), single-temperature blackbody (BBODY), and power-law component (POWERLAW). The other sources exhibited spectra consistent with hard state and are therefore modeled with a power-law component (CUTOFFPL) and single-temperature blackbody (BBODY) when needed.

When reflection features are present in the spectra, we utilize the self-consistent reflection model RELXILL (García et al. 2014) or the preliminarily flavor of this model tailored to thermal emission from an NS RELXILLNS (T. Dauser, J. A. García, & R. M. Ludlam 2019, in preparation). The major difference between these models is the illuminating continuum that provides the hard X-rays that shape the resulting reflection spectrum. RELXILL uses a cutoff power-law input spectrum whereas RELXILLNS assumes a blackbody is irradiating the disk. The model components of RELXILL are as follows: q_1 is the inner emissivity index, q_2 is the outer emissivity index, $R_{\rm break}$ is the break radius between the two emissivity indices, a is the dimensionless spin parameter, i is the inclination in degrees, R_{in} is the inner disk radius in units of the ISCO ($R_{\rm ISCO}$), $R_{\rm out}$ is the outer disk radius in units of gravitational radius ($R_g = GM/c^2$), Γ is the photon index of the input cutoff power-law, $\log \xi$ is the log of the ionization parameter, $A_{\rm Fe}$ is the iron abundance of the system normalized to the Sun, $E_{\rm cut}$ is the cutoff energy, $f_{\rm refl}$ is the reflection fraction, z is the redshift to the object, and norm represents the normalization of the model. RELXILLNS has similar parameters with the addition of $\log n$ ($\rm cm^{-3}$) to vary the density of the accretion disk and kT_{bb} (keV) for the input blackbody spectrum instead of Γ and $E_{\rm cut}$.

When using the reflection models we impose the following: a single emissivity index $q = q_1 = q_2$, a redshift of $z = 0$ since these are Galactic sources, a spin of $a = 0$ since most NS in LMXBs have $a \leqslant 0.3$ (Galloway et al. 2008; Miller et al. 2011) and the ISCO is a slowly varying function in this regime, and a large outer disk radius of $R_{\rm out} = 990\,R_g$. For reference, $1\,R_{\rm ISCO} = 6\,R_g$ for $a = 0$ (Bardeen et al. 1972). In the case of 4U 1702−429 and 4U 0614+091 where burst oscillations imply $a = 0.155$ and $a = 0.199$, the assumption of $a = 0$ is a marginal difference of $<0.7\,R_g$ for the position of the ISCO.

[9] http://pulsar.sternwarte.uni-erlangen.de/wilms/research/tbabs/

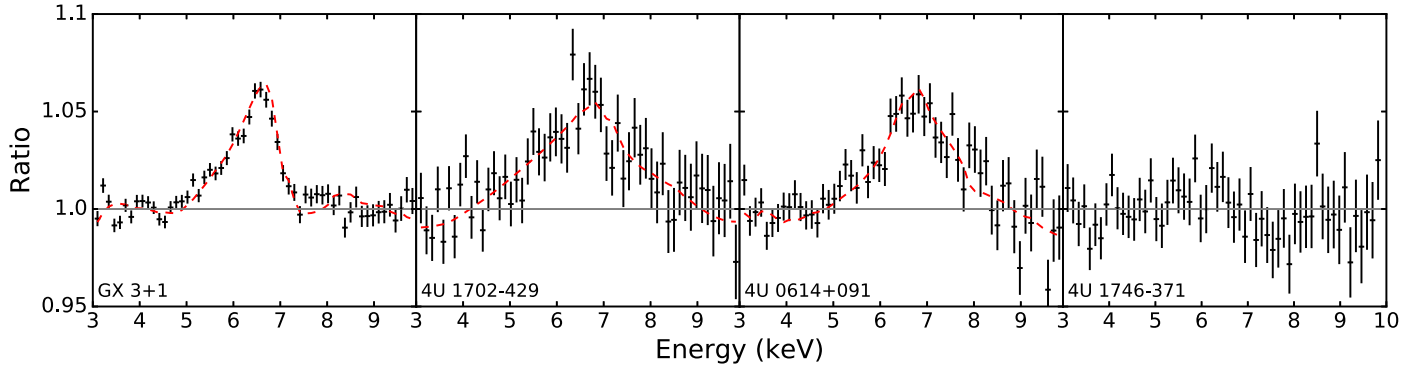

Figure 1. Ratio of the data to the continuum model for the atoll sources. The 5.0–8.0 keV energy band was ignored to prevent the Fe line region from skewing the fit. The dashed red line indicates the Fe line profile from the reflection continuum.

3.1. GX 3+1

The *NuSTAR* data were modeled in the 3.0–20.0 keV range. The continuum model includes a multitemperature blackbody, single-temperature blackbody, and power-law component. This provides a poor fit ($\chi^2/dof = 1491.4/135$) to the *NuSTAR* data due to the presence of reflection features that are not accounted for by this model. The Fe line profile from the data can be seen in Figure 1. We utilize the self-consistent thermal reflection model of RELXILLNS to properly describe these features. This improves the fit significantly to $\chi^2/dof = 199.0/128$ (15σ improvement via F-test), though this is still a poor statistical fit overall since the high S/N for this source places the data in the systematic and calibration limited regime. The power-law component is still statistically needed at the 9.5σ level of confidence. The disk blackbody normalization implies an incredibly small radius (~2.5 km), even after applying color corrections. This is likely to be a result of spectral hardening of pure blackbody emission by an atmosphere (London et al. 1986; Shimura & Takahara 1995; Merloni et al. 2000). We replace the DISKBB & POWER-LAW components with NTHCOMP, setting the photon seed input to a disk blackbody. This improves the overall fit further ($\Delta\chi^2 = 34.1$) implying a high optical depth of $\tau \sim 7$, but does not change the results for important parameters, i.e., $R_{\rm in}$ and inclination. The values for reflection model fitting are provided in Table 2. Note that RELXILLNS still contains a single-temperature blackbody continuum component in Model 2. The spectral components and ratio of the data to the overall model can be seen in panels (a) and (b) of Figure 2.

There is a flavor of RELXILL, known as RELXILLCP, that allows for reflection from a Comptonized disk component. This model has a hard-coded seed photon temperature of 0.05 keV. This is not appropriate for most NS spectral states, but it was recently employed successfully to model the accreting millisecond pulsar SAX J1808.4-3658 by Di Salvo et al. (2019). Since we find a low seed photon temperature of ~0.09 keV in our continuum fit with NTHCOMP, we attempt to use RELXILLCP instead of RELXILLNS. The overall model used in XSPEC is TBABS*(BBODY+RELXILLCP). This provides a significantly worse fit ($\chi^2/dof = 344.6/130$ or $>9\sigma$ worse). We show these results in Table 8 and Figure 4 of the Appendix, but do not report on it further.

3.2. 4U 1702−429

The *NuSTAR* data were modeled in the 3.0–50.0 keV energy band. The continuum is well described by a cutoff power law alone ($\chi^2/dof = 1162.4/388$), but there is a broad Fe line feature present in the ratio of the data to the continuum (Figure 1). In order to accommodate this feature, we apply the standard version of the self-consistent reflection model RELXILL. We initially fix the iron abundance at twice solar since the fit tended toward the maximum value of $A_{\rm Fe} = 10$. Applying the reflection model with $A_{\rm Fe} = 2$ provides a $\sim 17\sigma$ improvement in the overall fit ($\chi^2/dof = 526.6/383$) in comparison to the continuum only model. Last, we explore

Table 2
Reflection Modeling of GX 3+1

Model	Parameter	Model 1	Model 2
TBABS	$N_{\rm H}$ (10^{22} cm^{-2})	2.42[a]	2.42[a]
DISKBB	kT (keV)	$1.84^{+0.11}_{-0.01}$	...
	norm	$15.3^{+0.4}_{-2.7}$	...
POWERLAW	Γ	3.5 ± 0.1	...
	norm	$1.04^{+0.09}_{-0.02}$	...
NTHCOMP	Γ	...	$1.83^{+0.04}_{-0.01}$
	kT$_e$ (keV)	...	2.45 ± 0.04
	kT$_{bb}$ (keV)	...	$0.09^{+0.15}_{-0.08}$
	norm	...	0.86 ± 0.02
RELXILLNS	q	$3.2^{+0.1}_{-0.6}$	2.8 ± 0.5
	i(°)	28^{+3}_{-1}	25 ± 1
	$R_{\rm in}$ ($R_{\rm ISCO}$)	$1.8^{+0.2}_{-0.6}$	2.2 ± 0.2
	$R_{\rm in}$ (R_g)	$10.8^{+1.2}_{-3.6}$	13.2 ± 1.2
	kT_{bb} (keV)	$2.60^{+0.04}_{-0.02}$	1.6 ± 0.1
	log ξ	$2.75^{+0.05}_{-0.10}$	$3.2^{+0.1}_{-0.2}$
	$A_{\rm Fe}$	$0.62^{+0.17}_{-0.03}$	3 ± 2
	log n (cm^{-3})	$16.6^{+0.2}_{-0.3}$	$16.1^{+0.2}_{-0.1}$
	$f_{\rm refl}$	$0.93^{+0.04}_{-0.01}$	0.39 ± 0.07
	norm(10^{-3})	$0.72^{+0.05}_{-0.12}$	1.2 ± 0.2
	$F_{\rm unabs}$	8^{+1}_{-2}	6.5 ± 1.1
	L (10^{37} erg s^{-1})	$4.1^{+0.5}_{-1.0}$	3.3 ± 0.6
	$L/L_{\rm Edd}$	0.11	0.10
	χ^2 (dof)	199.0 (128)	164.9 (128)

Notes. Errors are reported at the 90% confidence level and calculated from Markov chain Monte Carlo (MCMC) of chain length 500,000. Data were fit in the 3.0–20.0 keV band. The outer disk radius was fixed at 990 R_g, the dimensionless spin parameter and redshift were set to zero for the RELXILLNS model. $f_{\rm refl}$ denotes the reflection fraction. The unabsorbed flux is taken in the 0.5–50.0 keV band and given in units of 10^{-9} erg s^{-1} cm^{-2}. Luminosity is calculated based upon a distance of $D_{\rm max} = 6.5$ kpc (Galloway et al. 2008).
[a] = fixed.

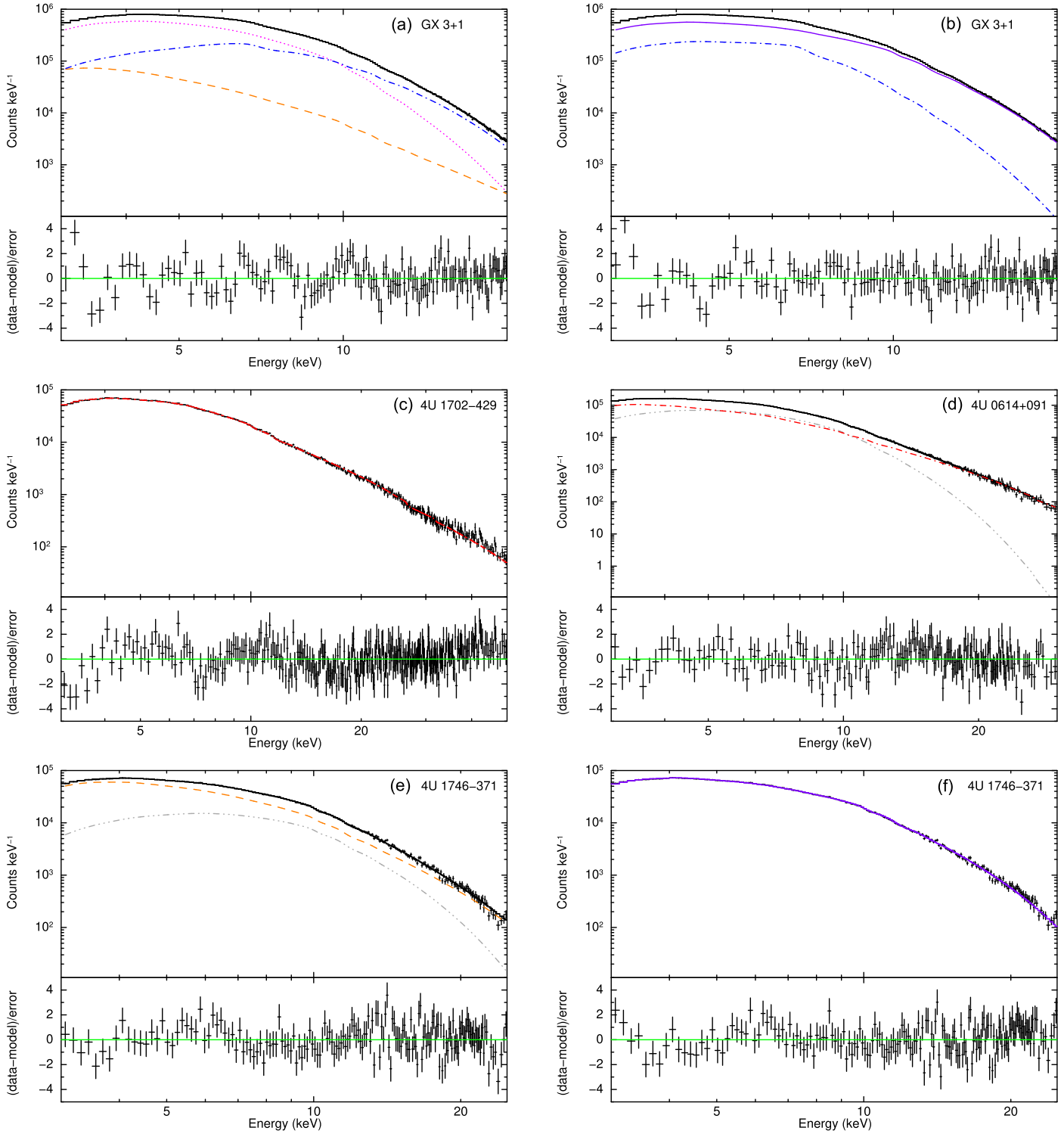

Figure 2. *NuSTAR* spectral modeling and residuals divided by errors for the sample of atoll sources. Dotted–dashed lines indicate the reflection model (blue: RELXILLNS, red: RELXILL). The magenta dotted line is a multitemperature blackbody to account for disk emission. The gray dotted–dotted-dotted–dashed line is a single-temperature blackbody to account for boundary layer emission. The orange dashed line indicates the power-law component. The purple solid line is the Comptonization model. See Tables 2–5 for component parameters.

the dependence on the iron abundance by allowing it to be a free parameter. The value is greater than 4.6 times the solar value, but the position of the inner disk is consistent with the fit that had a fixed $A_{\rm Fe}$. Both fits are reported in Table 3. This overabundance could be indicative of a higher density disk than the hard-coded value of 10^{15} cm^{-3} in RELXILL. We note that the model flavor RELXILLD provides the option of variable density in the disk. However, the current version of this model has a fixed cutoff energy of 300 keV, which is much higher than the value required to fit these data. Panel (c) of Figure 2 shows the model components and ratio of the *NuSTAR* fit with $A_{\rm Fe}$ left free to vary. Additionally, we also try fitting the

Table 3
Reflection Modeling of 4U 1702-429

Model	Parameter	Fixed A_{Fe}	Free A_{Fe}
TBABS	N_H (10^{22} cm^{-2})	2.32[a]	2.32[a]
RELXILL	q	$2.5^{+1.2}_{-0.3}$	$2.5^{+1.4}_{-0.1}$
	i(°)	59^{+5}_{-6}	61^{+2}_{-14}
	R_{in} (R_{ISCO})	$1.5^{+1.6}_{-0.4}$	$1.6^{+2.9}_{-0.1}$
	R_{in} (R_g)	$9.0^{+9.6}_{-2.4}$	$9.6^{+17.4}_{-0.6}$
	Γ	$1.97^{+0.02}_{-0.04}$	$1.97^{+0.02}_{-0.03}$
	log ξ	$3.74^{+0.25}_{-0.03}$	$4.02^{+0.33}_{-0.03}$
	A_{Fe}	2.0[a]	$4.9^{+4.6}_{-0.3}$
	E_{cut}	53^{+11}_{-2}	57^{+9}_{-4}
	f_{refl}	$0.57^{+0.92}_{-0.01}$	$0.5^{+0.1}_{-0.2}$
	norm (10^{-3})	$0.70^{+0.04}_{-0.30}$	$0.75^{+0.09}_{-0.05}$
	F_{unabs}	$0.58^{+0.03}_{-0.25}$	$0.57^{+0.07}_{-0.04}$
	L (10^{36} erg s^{-1})	$2.2^{+0.1}_{-0.9}$	$2.2^{+0.3}_{-0.1}$
	L/L_{Edd}	0.006	0.006
	χ^2 (d.o.f.)	526.6 (383)	480.2 (382)

Notes. Errors are reported at the 90% confidence level and calculated from Markov chain Monte Carlo (MCMC) of chain length 500,000. *NuSTAR* data were fit in the 3.0–50.0 keV band. The outer disk radius was fixed at 990 R_g, the dimensionless spin parameter and redshift were set to zero for the RELXILL model. f_{refl} denotes the reflection fraction. The unabsorbed flux is taken in the 0.5–50.0 keV band and given in units of 10^{-9} erg s^{-1} cm^{-2}. Luminosity is calculated based upon a distance of $D_{max} = 5.65$ kpc (Galloway et al. 2008).
[a] = fixed.

Table 4
Reflection Modeling of 4U 0614+091

Model	Parameter	*NuSTAR*
TBABS	N_H (10^{21} cm^{-2})	3.46[a]
BBODY	kT (keV)	$1.51^{+0.03}_{-0.01}$
	norm (10^{-3})	$3.55^{+0.04}_{-0.42}$
RELXILL	q	$2.07^{+0.50}_{-0.04}$
	i(°)	52^{+10}_{-2}
	R_{in} (R_{ISCO})	$1.3^{+5.4}_{-0.2}$
	R_{in} (R_g)	$7.8^{+32.4}_{-1.2}$
	Γ	$2.57^{+0.03}_{-0.24}$
	log ξ	$3.35^{+0.12}_{-0.06}$
	A_{Fe}	$0.58^{+0.86}_{-0.06}$
	E_{cut}	16^{+1}_{-4}
	f_{refl}	$1.0^{+0.3}_{-0.4}$
	norm (10^{-3})	$4.1^{+0.6}_{-1.1}$
	F_{unabs}	$2.2^{+0.3}_{-0.6}$
	L (10^{36} erg s^{-1})	$2.7^{+0.4}_{-0.7}$
	L/L_{Edd}	0.007
	χ^2 (d.o.f.)	249.8 (213)

Notes. Errors are reported at the 90% confidence level and calculated from Markov chain Monte Carlo (MCMC) of chain length 500,000. The data were fit in the 3.0–30.0 keV band. The outer disk radius was fixed at 990 R_g, the dimensionless spin parameter and redshift were set to zero for the RELXILL model. f_{refl} denotes the reflection fraction. The unabsorbed flux is taken in the 0.5–50.0 keV band and given in units of 10^{-9} erg s^{-1} cm^{-2}. Luminosity is calculated based upon a distance of $D_{max} = 3.2$ kpc (Kuulkers et al. 2010).
[a] = fixed.

spectrum with RELXILLCP, but do not find an improvement in the overall fit ($\Delta\chi^2$ increases by 4.7 for the same number of degrees of freedom). We present this in Table 8 and Figure 4 in the Appendix.

3.3. 4U 0614+091

The *NuSTAR* data were modeled in the 3.0–30.0 keV energy band. The column density was fixed at the value inferred from fitting the *XMM-Newton*/RGS of $N_H = 3.46 \times 10^{21}$ cm^{-2}. The continuum is consistent with the hard state, which is well described by a single-temperature blackbody and cutoff power law ($\chi^2/dof = 457.3/220$). There is a broad emission feature in the Fe K band that can be seen in Figure 1. We employ RELXILL to account for the reflected emission. This provides a $\sim 10\sigma$ improvement in the overall fit. Parameter values are given in Table 4. The spectrum and spectral components can be seen in panel (d) of Figure 2.

3.4. 4U 1746−371

The *NuSTAR* data were modeled in the 3.0–25.0 keV band. The column density along the line of sight is fixed at $N_H = 3.76 \times 10^{21}$ cm^{-2}. The spectrum can be entirely described by a cutoff power law and single-temperature blackbody component ($\chi^2/dof = 224.3/177$). There is not a strong detection of an Fe line component (see Figure 1). Applying a Gaussian component at 6.4 keV provides a marginal improvement of $\chi^2/dof = 211.3/175$ (or 2.8σ) with an equivalent width of $\sim$30 eV. Allowing the spectrum to be described by reflection with RELXILL provides an improvement in the fit ($\Delta\chi^2$ decreases by 17.7 for 2 dof). This is a 3.4σ improvement in comparison to the continuum only modeling. We fixed the following parameter values in the reflection model to those typical of other sources: $q = 3.2$ (Wilkins 2018), $R_{in} = 1R_{ISCO}$, $A_{Fe} = 1$, $\log(\xi) = 3.0$, and an inclination of $i = 75°$ (because it is a "dipping" source). We can then place an upper limit on the presence of reflection to be 13% from the reflection fraction. Allowing the fixed parameters within RELXILL to be free does not provide any meaningful constraints. For example, the inner disk radius is completely unconstrained (i.e., consistent with both hard-coded limits of $1\,R_{ISCO}$ and $100\,R_{ISCO}$). This was also the case for the ionization parameter, which was consistent with $\log\xi = 0$ and $\log\xi = 4.7$. We therefore are unable to learn more information about the reflected component.

The source is likely highly Comptonized. Switching out the continuum for Comptonization alone (NTHCOMP: Zdziarski et al. 1996; Zycki et al. 1999) provides a comparatively good fit ($\chi^2/dof = 226.4/178$) and implies a high optical depth of $\tau \sim 6$. Both continuum model fits are reported in Table 5. The spectrum and spectral components for each fit can be seen in panels (e) and (f) of Figure 2. We try to apply RELXILLCP to again check the presence of reflection in this observation. We fix the same parameters as the fit performed with RELXILL while allowing the continuum parameters, reflection fraction, and normalization to vary. This provides an improvement over the spectral modeling with NTHCOMP alone ($\Delta\chi^2 = 11$ for the same number of dof). We obtain a higher upper limit on the presence of reflection ($\sim$56%), but we are still unable to constrain reflection parameter values when they are allowed to vary. The combination of high inclination and strong Comptonization could be responsible for scattering any potential reflection features in this system out of the line of sight (see Figure 5 of Petrucci et al. 2001) and suggests we are

Table 5
Continuum Modeling of 4U 1746-371

Model	Parameter	Power-law	Comptonization
TBABS	$N_{\rm H}$ (10^{21} cm^{-2})	3.76[a]	3.76[a]
BBODY	kT (keV)	2.4 ± 0.2	⋯
	norm (10^{-4})	5.4 ± 0.9	⋯
CUTOFFPL	Γ	1.3 ± 0.2	⋯
	$E_{\rm cut}$	5.5 ± 0.7	⋯
	norm (10^{-2})	6.6 ± 0.7	⋯
NTHCOMP	Γ	⋯	1.91 ± 0.02
	$kT_{\rm e}$ (keV)	⋯	2.91 ± 0.04
	$kT_{\rm bb}$ (keV)	⋯	$0.50^{+0.04}_{-0.05}$
	norm (10^{-2})	⋯	$2.4^{+0.4}_{-0.3}$
	$F_{\rm unabs}$	0.45 ± 0.09	$0.34^{+0.06}_{-0.04}$
	L (10^{36} erg s^{-1})	8 ± 2	$5.8^{+1.0}_{-0.7}$
	$L/L_{\rm Edd}$	0.02	0.015
	χ^2 (d.o.f.)	224.3 (177)	226.4 (178)

Notes. Errors are reported at the 90% confidence level and calculated from Markov chain Monte Carlo (MCMC) of chain length 500,000. *NuSTAR* was fit in the 3.0–25.0 keV band. The unabsorbed flux is taken in the 0.5–50.0 keV band and given in units of 10^{-9} erg s^{-1} cm^{-2}. Luminosity is calculated based upon a distance of $D_{\rm max} = 11.9$ kpc (Pritzl et al. 2001).
[a] = fixed.

observing through the Comptonizing corona that is on top of the accretion disk.

4. Discussion

We perform a time-averaged spectral analysis with a focus on detecting reflection features in a sample of accreting atoll sources that were granted ∼20 ks observations per source with *NuSTAR* to determine the position of the inner disk. The sources span a range in Eddington fraction from 0.006–0.11 (assuming the empirical limit of 3.8×10^{38} erg s^{-1}). Broad Fe lines were detected in three out of four of the sources: GX 3+1, 4U 1702−429, and 4U 0614+091. We account for reflection by using different flavors of RELXILL based on the illuminating continuum in these systems. There are other families of reflection models, such as REFLIONX (Ross & Fabian 2005) or BBREFL (Ballantyne 2004), but Ludlam et al. (2017a) demonstrated that reflection fitting with these models provides similar results as RELXILL. The final source, 4U 1746−371, does not require reflection in order to describe the spectrum. However, we can place an upper limit on its presence through the reflection fraction to be 13%–56% depending on the choice of the illuminating continuum. The ionization parameters of the three sources with reflection are consistent with $\log \xi = 2.3$–4.0 seen in other NS LMXBs (Cackett et al. 2010; Ludlam et al. 2017a).

GX 3+1 displayed a particularly soft spectrum that was well described by a double thermal model with a power-law component. The reflection model determined the accretion disk was truncated prior to the ISCO at $1.8^{+0.2}_{-0.6}\ R_{\rm ISCO}$ ($10.8^{+1.2}_{-3.6}\ R_g$) and inclination of 27°–31°. The inner disk position agrees with the $\sim 10\ R_g$ limit found by Pintore et al. (2015), but the inclination is slightly lower than previous investigations with *XMM-Newton* by Piraino et al. (2012) and Pintore et al. (2015). A potential source of the discrepancy between the measured inclinations could be due to the difference in $N_{\rm H}$ used when performing spectral fits. The choice of absorption model used (e.g., WABS, PHABS, TBABS, etc.), as well as abundances and cross-sections adopted can result in changes in the measured $N_{\rm H}$ by up to 30% (E. Gatuzz & J. A. García, 2019, in preparation). This can alter the edge at 7 keV in the Fe line region, which can impact the blue wing predicted by the reflection model when fitting, and therefore lead to changes in the inferred inclination. Additionally, we obtain similar values for $R_{\rm in}$ and inclination when using a Comptonized disk blackbody component for the continuum.

The position of the inner disk was close to the ISCO for 4U 1702−429, though the large error bars are also compatible with disk truncation. This is in agreement with the values reported in Mazzola et al. (2019) from archival *XMM-Newton*, *INTEGRAL*, and *BeppoSAX* observations. The iron abundance had to be fixed during the reflection fits. Allowing the iron abundance to vary required >5× the solar abundance. This improved the fit, but the disk was highly ionized ($\log \xi \simeq 4$). The super-solar abundance likely indicates that the disk has a higher density than accounted for by the RELXILL model (10^{15} cm^{-3}). This behavior was also seen for the BH HMXB Cyg X-1 (Tomsick et al. 2018), which had a super-solar Fe abundance when modeled with a disk density of 10^{15} cm^{-3}. When the disk density was allowed to increase, the Fe abundance in the reflection model decreased. See García et al. (2018) for a recent discussion on the relationship between disk density and inferred Fe abundance. The inclination is between 53° and 64° depending on the value of $A_{\rm Fe}$, in agreement with the results from Iaria et al. (2016) from *XMM-Newton* and *INTEGRAL* data. Additionally, the upper limits on the inner disk position when $A_{\rm Fe} = 2.0$ are consistent with the values reported in Iaria et al. (2016).

4U 0614−091 was also truncated slightly outside of the ISCO. The subsolar Fe abundance agrees with previous studies and the nature of the donor in this system (Madej et al. 2010, 2014), although the abundance is consistent with solar at the 90% confidence level. The inclination of the system from RELXILL is 50°–62°, which again agrees with the results from the *XMM-Newton* RGS and EPIC-pn studies performed by Madej et al. (2010, 2014). This supports the idea that relativistically blurred Fe and O lines can originate from very similar regions in the disk providing additional diagnostics for the inner accretion flow in these systems (Ludlam et al. 2016). Future studies conducted with observatories such as *NICER* (Gendreau et al. 2012) that are sensitive to Fe lines and lower energy emission features simultaneously can confirm if these locations are the same or mutually exclusive.

Further observations of 4U 1702−429 and 4U 0614−091 would yield tighter constraints on the position of the inner disk radius to determine if the accretion flow is truncated or close to the NS, particularly if 4U 1702−429 is targeted in a state with higher intensity. Additionally, the development of a cutoff power-law reflection model with variable disk density and cutoff energy will shed light on the peculiar super-solar iron abundances implied in the reflection fitting of 4U 1702−429. The current version of RELXILLD that allows for variable disk density has a fixed cutoff energy of 300 keV.

4U 1746−371 did not show a clear signature of reflection in its spectrum. The low cutoff energy is consistent with cutoff energies seen in other NS LMXBs in intermediate states (4U 1636−536, 4U 1705−44, 4U 1728−34, 4U 1734−44, and 4U 1820−30: Church et al. 2014) and an *INTEGRAL* study of this source by Balman (2009). Although, we find a hotter

blackbody component and harder spectral index in comparison to Balman (2009). The spectral index is closer to the value of $\Gamma = 1.20 \pm 0.27$ found in Church & Bałucińska-Church (2001). Additionally, we model the continuum emission with a Comptonized accretion disk component. The optically thick Comptonized component ($\tau \sim 6$) and low electron temperature ($\sim$3 keV) of 4U 1746−371 is akin to GX 13+1 (Iaria et al. 2014; D'Aì et al. 2014), which is another highly inclined "soft" atoll. In contrast to 4U 1746−371, GX 13+1 continuously shows a broad Fe line component and narrow Fe absorption features indicative of winds (Díaz Trigo et al. 2012). This could be due to the fact that Fe line flux is correlated with continuum flux (Lin et al. 2010) and GX 13+1 is more than six times as luminous (D'Aì et al. 2014). A simple Gaussian at 6.4 keV to account for a potential Fe line component in 4U 1746−371 gave an equivalent width of $\sim$30 eV, which is about one-sixth of the value reported in Díaz Trigo et al. (2006). However, the observation reported in Díaz Trigo et al. (2006) occurred when the source was a factor of four times more luminous. The discrepancy in the equivalent width of the Fe line component is likely the result of a change in ionization state, though we were unable to place any meaningful constraints on the ionization parameter with RELXILL or RELXILLCP.

Another source was recently found to not have reflection features present in its persistent spectrum: the Z source GX 5−1 (Homan et al. 2018). The likeliest explanation for the absence of reflection features was a highly ionized disk given the source's high luminosity ($L_{1-100\ \mathrm{keV}} = 2.97 \times 10^{38}$–$4.27 \times 10^{38}$ erg s^{-1}). A highly ionized accretion disk could explain the lack of reflection in 4U 1746−371, but the source is not nearly as luminous as GX 5−1. 4U 1746−371 was at 0.02 L_{Edd} at the time of the *NuSTAR* observation, whereas GX 5−1 spanned the range of $\sim$0.76–1.14 L_{Edd}. Since 4U 1746−371 is a known dipping source, it is more likely that the combination of source geometry and Comptonization in the accretion disk corona scatters reflected photons out of the line of sight vastly reducing the number of line contributing photons (Petrucci et al. 2001). This is further supported by the high optical depth ($\tau \sim 6$) from the Comptonization fit in addition to the dipping nature of the source. Note that this is not the case for GX 3+1 since the source is at a lower inclination and we are not looking through the Comptonizing corona on top of the accretion disk. However, this could also explain the lack of a reflection spectrum in the "soft" state for GS 1826−24, which presents evidence of being highly inclined and Comptonized as well (Chenevez et al. 2016).

For the three sources in which reflection was detected, the brightest of the sources is truncated prior to the ISCO whereas the lower Eddington luminosities have inner disk radii nearly consistent with the ISCO, within errors. We are able to place these three sources into the larger sample sof NSs (with $B < 10^{10}$ G) that have been observed with *NuSTAR* wherein reflection allows limits to be placed on the location of the disk. Table 6 and Figure 3 are updated from Ludlam et al. (2017a) to incorporate recent analyses and further division into NS subclasses (persistent atoll and Z sources, transients, and a very faint X-ray binary). The Eddington fraction, which is a proxy for $\dot{m}$, is calculated from the 0.5–50 keV luminosity of each source divided by the empirical Eddington limit of 3.8×10^{38} erg s^{-1}. The observations of 4U 1702−429 and 4U 0614+091 in this work provide the lowest luminosity disk position measurements for persistent atoll sources observed with *NuSTAR*. In the case of the very faint X-ray binary, IGR J17062−6143 is able to constantly accrete at very low $\dot{m}$ where the disk may enter the radiatively inefficient accretion flow (RIAF) regime (Narayan & Yi 1994; Blandford & Begelman 1999), but truncation by the magnetosphere is not ruled out (van den Eijnden et al. 2018).

Table 6
NS Inner Disk Radii and Eddington Fraction Observed with *NuSTAR*

Source	R_{in} (ISCO)	F_{Edd}	References
Atolls			
Ser X-1	1.03–1.20	0.34	1
	1.76–2.70	0.34	2
4U 1705−44	1.46–1.93	0.10	3
4U 1636−53	1.00–1.14	0.01	3
4U 1728−34	1.0–2.0	0.04	4
GX 3+1	1.2–2.0	0.11	⋯
4U 1702−429	1.1–3.1	0.006	⋯
4U 0614+091	1.1–5.7	0.007	⋯
Z			
GX 17+2	1.00–1.30	0.57	3
Cyg X-2	2.5–6.1	0.47	5
GX 349+2	2.71–2.96	0.54	6
	3.53–4.18	0.53	6
	2.45–2.88	0.60	6
	2.72–3.2	0.70	6
Transients			
4U 1608−52	1.3–2.0	0.03	7
1RXS J180408.9-34	1.00–1.85	0.02	8
	1.0–1.5	0.10	9
Aquila X-1	2.3–3.1	0.07	10
	1.9–2.4	0.23	10
XTE J1709−267	2.0–2.8	0.04	11
MXB 1730−335	6.08–8.08	0.025	12
VFXB			
IGR J17062−6143	9.8–16.5	$\sim$0.003	13

Note. (1) Miller et al. (2013); (2) Matranga et al. (2017); (3) Ludlam et al. (2017a); (4) Sleator et al. (2016); (5) Mondal et al. (2018); (6) Coughenour et al. (2018); (7) Degenaar et al. (2015); (8) Ludlam et al. (2016); (9) Degenaar et al. (2016); (10) Ludlam et al. (2017c); (11) Ludlam et al. (2016); (12) van den Eijnden et al. (2017); (13) van den Eijnden et al. (2018).

It should be noted that the R_{in} estimates for Serpens X-1 by Miller et al. (2013) and Matranga et al. (2017) used the same *NuSTAR* data set; however, Matranga et al. (2017) also used *XMM-Newton* observations to construct a broadband X-ray spectrum. This emphasizes the importance of the lower-energy bandpass in deriving reflection parameters. Hence values in Table 6 and Figure 3 may be biased since *NuSTAR* only has the high energy coverage. Regardless, the lack of a clear trend between F_{Edd} and R_{in} reaffirms the previously reported complex behavior of the disk over various mass accretion rates (Cackett et al. 2010; D'Aì et al. 2010; Ludlam et al. 2017a) and suggests the presence of a boundary layer or that the magnetic field of the NS likely plays a role.

In Table 7 we provide estimates for the extent of a boundary layer using Equation (25) from Popham & Sunyaev (2001) and upper limits on the magnetic field strength using Equation (1) from Cackett et al. (2009) for these systems. The large upper

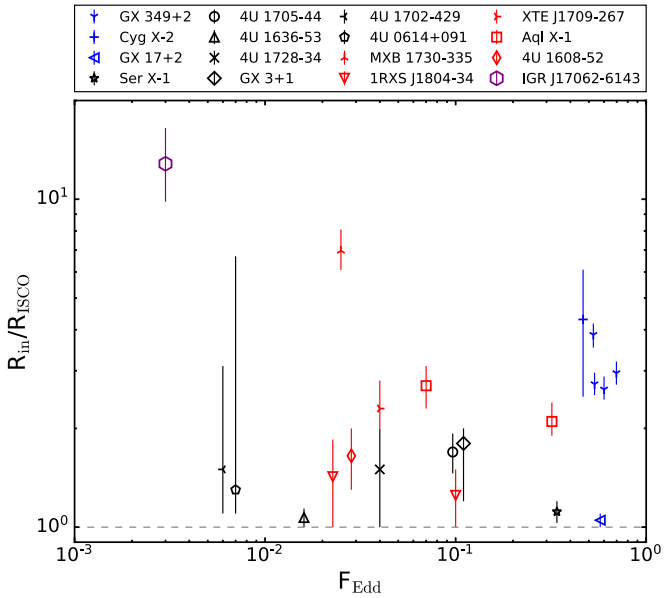

Figure 3. Comparison of Eddington fraction and measured inner disk radii for NSs observed with *NuSTAR*. Black points indicate persistent atoll sources, blue points indicate persistent Z sources, red points are transient systems, and the purple point indicates a very faint X-ray binary (VFXB). The dashed gray line denotes the innermost stable circular orbit. See Table 6 for inner disk radii and Eddington fractions.

Table 7
Maximum Boundary Layer Extent and Magnetic Field Strength

Source	$R_{BL,max}$ (R_g)	B_{max} (10^8 G)
GX 3+1	∼6.67	⩽6.7
4U 1702−429	∼5.35	⩽3.3
4U 0614+091	∼5.36	⩽14.5

Note. The maximum radial extent of the boundary layer region is calculated based up the maximum luminosity reported in Tables 2–4. We assume a canonical NS ($M_{NS} = 1.4M_{\odot}$, $R_{NS} = 10$ km). For the estimate of the upper limit on the magnetic field strength at the poles, we use the maximum unabsorbed 0.5–50 keV flux and inner disk radius from the *NuSTAR* fits. Additionally, we assume an angular anisotropy and conversion factor of unity (Cackett et al. 2009). The efficiency of accretion in both calculations is assumed to be 0.2 (Sibgatullin & Sunyaev 2000).

limit on the magnetic field strength for 4U 0614+091 is driven by the large uncertainty on the inner disk radius. Although we do not detect pulsations during these observations, the sources could still be magnetically accreting. The hot spot could be nearly aligned with the spin axis, in which case pulsations would be undetectable, or the modulated emission could be scattered by the circumstellar gas (Lamb et al. 1985). A comprehensive explanation regarding all the ways pulsations are suppressed or hidden from view in NS LMXBs can be found in Lamb et al. (2009). The extent of the boundary layer regions are too small to account for the disk position, but these values may be underestimated as they do not account for spin and viscous effects in this layer. An additional plausible explanation for disk truncation could be that the innermost region of the accretion disk has given way to a compact Comptonizing coronal region as expected in lower luminosity regimes (Narayan & Yi 1994; Done et al. 2007; Veledina et al. 2013). We are unable to determine the exact truncation mechanism from a single observation. This is because the position of the disk as a function of $\dot{m}$ changes in opposing manners for truncation by the magnetosphere (Ibragimov & Poutanen 2009) or a boundary layer extending from the NS surface (Popham & Sunyaev 2001). Multiple observations over significant changes in mass accretion rate within individual sources are needed to determine the definitive truncation mechanism for a system.

5. Summary

We present a spectral analysis of four persistent atoll sources observed with *NuSTAR* to investigate the location of the inner disk measured via reflection fitting techniques within these relatively low luminosity systems. We detect the presence of reflection firmly in three out of four of these sources (GX 3+1, 4U 1702−429, and 4U 0614+091). Reflection features were not detected in 4U 1746−371 likely due to a combination of source geometry and strong Comptonization. These sources span a range in Eddington fraction of 0.006–0.11, providing the lowest F_{Edd} disk position measurement for an atoll source observed with *NuSTAR*, and increase the number of sources with detected reflection features by ∼20% for the *NuSTAR* sample. Adding these sources to the existing sample of NSs with inner radius measurements reaffirms the lack of a clear one-to-one trend between the position of the inner disk and mass accretion rate as observed with other X-ray missions such as *XMM-Newton* and *Suzaku* (e.g., Cackett et al. 2010; D'Aì et al. 2010; Chiang et al. 2016b). This emphasizes the need to shift focus to investigate the truncation mechanisms in individual sources to determine the dynamical role of the boundary layer or magnetosphere. In order to disentangle these different scenarios of disk truncation, multiple observations of a source over a large range in mass accretion rate are necessary.

We thank the referee for their comments that have improved this work. This research has made use of the NuSTAR Data Analysis Software (NuSTARDAS) jointly developed by the ASI Science Data Center (ASDC, Italy) and the California Institute of Technology (Caltech, USA). R.M.L. is funded through a NASA Earth and Space Science Fellowship. E.M.C. gratefully acknowledges NSF CAREER award AST-1351222. We thank J. van den Eijnden for verifying the unabsorbed flux of IGR J17062−6143.

Appendix
Spectral Fitting with Relxillcp

Here we provide the reader with the results from using the model RELXILLCP on GX 3+1 and 4U 1702−429. This model produces reflection from the reprocessing of photons from a Comptonized disk component with a hard-coded seed photon temperature of 0.05 keV. Table 8 provides the parameter values that can be compared to the resulting fits in Tables 2 and 3 for GX 3+1 and 4U 1702−429, respectively. Figure 4 is given to provide a direct comparison to the fits presented in Figure 2. These fits do not provide an improvement in the overall fit of the spectra from the results presented in Section 3.1 and Section 3.2. In the case of 4U 1702−429, the comparable fit with high A_{Fe} and ionization still supports the need for higher disk density models.

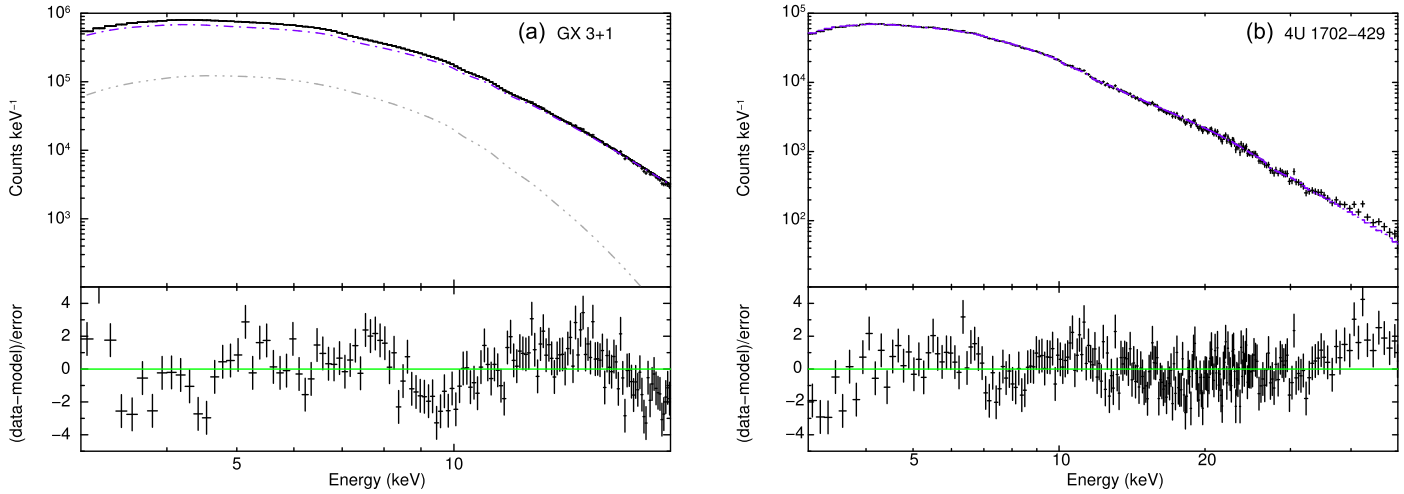

Figure 4. *NuSTAR* spectral modeling and residuals divided by errors for (a) GX 3+1 and (b) 4U 1702−429 when fit with RELXILLCP. The purple dotted–dashed lines indicate RELXILLCP, which contains both the Comptonized disk component of the continuum and reflection. The gray dot-dot-dotted–dashed line is a single-temperature blackbody to account for boundary layer emission.

Table 8
Reflection Modeling with RELXILLCP

Model	Parameter	GX 3+1	4U 1702−429
TBABS	$N_{\rm H}$ (10^{22} cm^{-2})	2.42[a]	2.32[a]
BBODY	kT (keV)	1.40 ± 0.02	⋯
	norm (10^{-3})	6.8 ± 0.3	⋯
RELXILLCP	q	3.1 ± 0.3	2.3 ± 0.2
	$i(^\circ)$	24 ± 1	64 ± 1
	R_{in} ($R_{\rm ISCO}$)	$1.85^{+0.35}_{-0.27}$	$1.00^{+0.4}_{*}$
	R_{in} (R_g)	$10.8^{+2.1}_{-1.6}$	$6.0^{+2.4}_{*}$
	Γ	$1.72^{+0.03}_{-0.01}$	2.00 ± 0.01
	$\log \xi$	$3.30^{+0.01}_{-0.05}$	$4.7^{*}_{-0.1}$
	$A_{\rm Fe}$	$10^{*}_{-0.2}$	$8.7^{+0.7}_{-0.9}$
	kT (keV)	2.24 ± 0.01	20^{+2}_{-1}
	$f_{\rm refl}$	$0.66^{+0.03}_{-0.07}$	$2.6^{+0.4}_{-0.5}$
	norm (10^{-3})	7.2 ± 0.1	$0.30^{+0.02}_{-0.07}$
	χ^2(dof)	344.6 (130)	484.9 (382)

Notes. Errors are reported at the 90% confidence level. An asterisk indicates that the parameter is at the hard-coded limit of the model. The outer disk radius was fixed at 990 R_g, the dimensionless spin parameter and redshift were set to zero for the RELXILLCP model. $f_{\rm refl}$ denotes the reflection fraction.
[a] = fixed.

ORCID iDs

R. M. Ludlam https://orcid.org/0000-0002-8961-939X
D. Barret https://orcid.org/0000-0002-0393-9190
E. M. Cackett https://orcid.org/0000-0002-8294-9281
B. M. Coughenour https://orcid.org/0000-0003-0870-6465
J. A. García https://orcid.org/0000-0003-3828-2448

References

Arnaud, K. A. 1996, in ASP Conf. Ser.101, Astronomical Data Analysis Software and Systems V, ed. G. H. Jacoby & J. Barnes (San Francisco, CA: ASP), 17
Asai, K., Dotani, T., Nagase, F., & Mitsuda, K. 2000, ApJS, 131, 571
Ballantyne, D. R. 2004, MNRAS, 351, 57
Balman, Ş. 2009, ApJ, 138, 50
Bałucińska-Church, M., Church, M. J., & Smale, A. P. 2004, MNRAS, 347, 334
Bardeen, J. M., Press, W. H., & Teukolsky, S. A. 1972, ApJ, 178, 347
Blandford, R. D., & Begelman, M. C. 1999, MNRAS, 303, L1
Braje, T. M., Romani, R. W., & Rauch, K. P. 2000, ApJ, 531, 447
Brandt, S., Castro-Tirado, A. J., Lund, N., et al. 1992, A&A, 262, L15
Cackett, E. M., Altamirano, D., Patruno, A., et al. 2009, ApJL, 694, L21
Cackett, E. M., Miller, J. M., Ballantyne, D. R., et al. 2010, ApJ, 720, 205
Cackett, E. M., Miller, J. M., Bhattacharyya, S., et al. 2008, ApJ, 674, 415
Chenevez, J., Falanga, M., Brandt, S., et al. 2006, A&A, 449, L5
Chenevez, J., Galloway, D. K., in't Zand, J. J. M., et al. 2016, ApJ, 818, 135
Chiang, C.-Y., Cackett, E. M., Miller, J. M., et al. 2016a, ApJ, 821, 105
Chiang, C.-Y., Morgan, R. A., Cackett, E. M., et al. 2016b, ApJ, 831, 45
Choudhury, K., García, J. A., Steiner, J. F., & Bambi, C. 2017, ApJ, 851, 57
Church, M. J., & Bałucińska-Church, M. 2001, A&A, 369, 915
Church, M. J., Gibiec, A., & Bałucińska-Church, M. 2014, MNRAS, 438, 2784
Cook, G. B., Shapiro, S. L., & Teukolsky, S. A. 1994, ApJ, 424, 823
Coughenour, B. M., Cackett, E. M., Miller, J. M., & Ludlam, R. M. 2018, ApJ, 867, 64
D'Aì, A., Di Salvo, T., Ballantyne, D., et al. 2010, A&A, 516, A36
D'Aì, A., Iaria, R., Di Salvo, T., et al. 2014, A&A, 564, A62
Degenaar, N., Altamirano, D., Parker, M., et al. 2016, MNRAS, 461, 4049
Degenaar, N., Miller, J. M., Chakrabarty, D., et al. 2015, MNRAS, 451, L85
Deutsch, E. W., Anderson, S. F., Margon, B., & Downes, R. 1998, ApJ, 493, 775
Di Salvo, T., Sanna, A., Burderi, L., et al. 2019, MNRAS, 483, 767
Díaz Trigo, M., Parmar, A. N., Boirin, L., Mendez, M., & Kaastra, J. 2006, A&A, 445, 179
Díaz Trigo, M., Sidoli, L., Boirin, L., & Parmar, A. N., M. 2012, A&A, 543, A50
Done, C., Gierliński, M., & Kubota, A. 2007, A&ARv, 15, 1
Fabian, A. C., Rees, M. J., Stella, L., & White, N. E. 1989, MNRAS, 238, 729
Galloway, D. K., Muno, M. P., Hartman, J. M., Psaltis, D., & Chakrabarty, D. 2008, ApJS, 179, 360
García, J. A., Dauser, T., Lohfink, A., et al. 2014, ApJ, 782, 76
García, J. A., Kallman, T. R., Bautista, M., et al. 2018, arxiv:1805.00581
Gendreau, K. C., Arzoumanian, Z., & Okajima, T. 2012, Proc. SPIE, 8443, 13
Gladstone, J., Done, C., & Gierliński, M. 2007, MNRAS, 378, 13
González Martínez-País, I., Shahbaz, T., & Casares Velázquez, J. 2014, Accretion Processes in Astrophysics (Cambridge: Cambridge Univ. Press)
Harrison, F. A., Craig, W. W., Christensen, F. E., et al. 2013, ApJ, 770, 103
Hasinger, G., & van der Klis, M. 1989, A&A, 225, 79
Homan, J., Steiner, J. F., Lin, D., et al. 2018, ApJ, 853, 157
Homan, J., van der Klis, M., Fridriksson, J. K., et al. 2010, ApJ, 719, 201
Iaria, R., Di Salvo, T., Burderi, L., et al. 2014, A&A, 561, 99
Iaria, R., Di Salvo, T., Del Santo, M., et al. 2016, A&A, 596, 21
Ibragimov, A., & Poutanen, J. 2009, MNRAS, 400, 492
King, A. L., Tomsick, J. A., Miller, J. M., et al. 2016, ApJL, 819, L29
Kuulkers, E. 2002, A&A, 383, L5
Kuulkers, E., den Hartog, P. R., in't Zand, J. J. M., et al. 2003, A&A, 399, 663
Kuulkers, E., in't zand, J. J. M., Atteia, J.-L., et al. 2010, A&A, 514, A65
Kuulkers, E., & van der Klis, M. 2000, A&A, 356, L45
Lamb, F. K., Boutloukos, S., Van Wassenhove, S., et al. 2009, ApJ, 706, 417

Lamb, F. K., Shibazaki, N., Alpar, M. A., & Shaham, J. 1985, Natur, 317, 681
Lin, D., Remillard, R. A., & Homan, J. 2007, ApJ, 667, 1073
Lin, D., Remillard, R. A., & Homan, J. 2010, ApJ, 719, 1350
London, R. A., Taam, R. E., & Howard, W. M. 1986, ApJ, 306, 170L
Ludlam, R. M., Miller, J. M., Bachetti, M., et al. 2017a, ApJ, 836, 140
Ludlam, R. M., Miller, J. M., Cackett, E. M., et al. 2016, ApJ, 824, 37
Ludlam, R. M., Miller, J. M., Cackett, E. M., Degenaar, N., & Bostrom, A. C. 2017b, ApJ, 838, 79
Ludlam, R. M., Miller, J. M., Degenaar, N., et al. 2017c, ApJ, 847, 135
Madej, O. K., García, J., Jonker, P. G., et al. 2014, MNRAS, 442, 1157
Madej, O. K., Jonker, P. G., Fabian, A. C., et al. 2010, MNRAS, 407, L11
Makishima, K., Mitsuda, K., Inoue, H., et al. 1983, ApJ, 267, 310
Markwardt, C. B., Strohmayer, T. E., & Swank, J. H. 1999, ApJL, 512, L125
Matranga, M., Di Salvo, T., Iaria, R., et al. 2017, A&A, 600, A24
Mazzola, S. M., Iaria, R., Di Salvo, T., et al. 2019, A&A, 621, 89
Merloni, A., Fabian, A. C., & Ross, R. R. 2000, MNRAS, 313, 193
Miller, J. M., Cackett, E. M., & Reis, R. C. 2009, ApJL, 707, L77
Miller, J. M., Maitra, D., Cackett, E. M., Bhattacharyya, S., & Strohmayer, T. E. 2011, ApJL, 731, L7
Miller, J. M., Parker, M. L., Fuerst, F., et al. 2013, ApJL, 779, L2
Mitsuda, K., Inoue, H., Koyama, K., et al. 1984, PASJ, 36, 741
Mondal, A. S., Dewangan, G. C., Pahari, M, & Raychaudhuri, B. 2018, MNRAS, 474, 2064
Narayan, R., & Yi, I. 1994, ApJL, 428, L13
Nelemans, G., Jonker, P. G., Marsh, T. R., & van der Klis, M. 2004, MNRAS, 348, L7
Oosterbroek, T., Barret, D., Guainazzi, M., & Ford, E. C. 2001, A&A, 366, 138
Papitto, A., Di Salvo, T., D'Aí, A., et al. 2009, A&A, 493, L39
Parmar, A. N., Stella, L., & Giommi, P. 1989, A&A, 222, 96
Petrucci, P. O., Merloni, A., Fabian, A., Haardt, F., & Gallo, E. 2001, MNRAS, 328, 501
Pintore, F., Di Salvo, T., Bozzo, E., et al. 2015, MNRAS, 450, 2016
Piraino, S., Santangelo, A., Kaaret, P., et al. 2012, A&A, 542, L27
Popham, R., & Sunyaev, R. 2001, ApJ, 547, 355
Pritzl, B. J., Smith, H. A., Catelan, M., & Sweigart, A. V. 2001, ApJ, 122, 2600
Ross, R. R., & Fabian, A. C. 2005, MNRAS, 358, 211
Sansom, A. E., Dotani, T., Asai, K., & Lehto, H. J. 1993, MNRAS, 262, 429
Shahbaz, T., Watson, C. A., Zurita, C., Villaver, E., & Hernandez-Peralta, H. 2008, PASP, 120, 848
Shimura, T., & Takahara, F. 1995, ApJ, 445, 780
Sibgatullin, N. R., & Sunyaev, R. A. 2000, AstL, 26, 699
Sleator, C. C., Tomsick, J. A., King, A. L., et al. 2016, ApJ, 827, 134
Strohmayer, T. E., Markwardt, C. B., & Kuulkers, E. 2008, ApJL, 672, L37
Swank, J. H., Becker, R. H., Pravdo, S. H., Saba, J. R., & Serlemitsos, P. J. 1976, IAUC, 3010, 1
Swank, J. H., Boldt, E. A., Holt, S. S., Serlemitsos, P. J., & Becker, R. H. 1978, MNRAS, 182, 349
Sztajno, M., Fujimoto, M. Y., van Paradijs, J., et al. 1987, MNRAS, 226, 39
Tomsick, J. A., Parker, M. L., García, J. A., et al. 2018, ApJ, 855, 3
van den Eijnden, J., Bagnoli, T., Degenaar, N., et al. 2017, MNRAS, 466, 98
van den Eijnden, J., Degenaar, N., Pinto, C., et al. 2018, MNRAS, 475, 2027
van der Klis, M. 2005, NATO Adv. Sci. Inst. Ser. B, 210, 283
Veledina, A., Poutanen, J., & Vurm, I. 2013, MNRAS, 430, 3196
Verner, D. A., Ferland, G. J., Korista, K. T., & Yakovlev, D. G. 1996, ApJ, 465, 487
Wijnands, R., Parikh, A. S., Altamirano, D., Homan, D., & Degenaar, N. 2017, MNRAS, 472, 559
Wilkins, D. R. 2018, MNRAS, 475, 748
Wilms, J., Allen, A., & McCray, R. 2000, ApJ, 542, 914
Zdziarski, A. A., Johnson, W. N., & Magdziarz, P. 1996, MNRAS, 283, 193
Zycki, P. T., Done, C., & Smith, D. A. 1999, MNRAS, 309, 561